THESIS FOR THE DEGREE OF LICENTIATE OF ENGINEERING

Corrosion and fracture in reinforced mortars with limestone calcined clay cement

TALLES FELIX

CHALMERS
UNIVERSITY OF TECHNOLOGY

Department of Architecture and Civil Engineering
Division of Structural Engineering
CHALMERS UNIVERSITY OF TECHNOLOGY

Gothenburg, Sweden 2026

Corrosion and fracture in reinforced mortars with limestone calcined clay cement
TALLES FELIX

Thesis for the degree of Licentiate of Engineering
Technical Report ACE-2026:6

Division of Structural Engineering
Department of Architecture and Civil Engineering
Chalmers University of Technology
SE-412 96 Gothenburg
Sweden
Telephone: +46 (0)31-772 1000

Cover
The cover image depicts a steel-reinforced Limestone Calcined Clay (LC^3) mortar specimen with visible corrosion-induced cracking and rust staining.

Printed by Chalmers Reproservice
Gothenburg, Sweden 2026

Corrosion and fracture in reinforced mortars with limestone calcined clay cement
Thesis for the degree of Licentiate of Engineering

TALLES FELIX

Department of Architecture and Civil Engineering
Division of Structural Engineering
Chalmers University of Technology

Abstract

Low-carbon substitutes for conventional cementitious binders, such as Limestone Calcined Clay Cement (LC^3), represent a promising pathway toward more sustainable infrastructure. However, their use in steel-reinforced concrete requires confidence in their long-term resistance to corrosion-related damage. This study examines the relationship between corrosion-induced cracking, mechanical behavior, and binder composition in mortars made with Ordinary Portland Cement (OPC) and LC^3, each represented by two strength classes.

Corrosion was accelerated using an impressed current technique. To evaluate the corrosion level leading to cracking, the applied electrical current was identical and constant for all specimens, and the resulting time-to-cracking, t_{crack}, was determined. The results were analyzed in relation to compressive strength, tensile strength, fracture energy, and the chloride migration coefficient.

LC^3 mortars exhibited a lower capacity to accommodate the expansive stresses generated by corrosion products, leading to earlier cracking than OPC mortars. This behavior is consistent with the measured fracture energy, which was lower for LC^3 mixes, indicating a reduced resistance to crack propagation despite comparable strength levels.

Nonlinear finite element analyses were performed using the measured material properties and a corrosion model based on radial expansion at the steel-concrete interface to support and interpret the experimental observations. The simulations reproduced the relative cracking trends among the mortars, although cracking was predicted later than observed experimentally. Nevertheless, normalized results captured the ranking of the mixtures, supporting the modeling approach while indicating the need for improved calibration of the corrosion expansion properties.

Overall, the results suggest a potential mechanical drawback of LC^3 mortars in reinforced systems. However, this may be partly compensated by their enhanced resistance to chloride ingress and delayed corrosion initiation under natural exposure conditions. These findings emphasize the importance of comprehensive durability assessments that extend beyond corrosion initiation to include the mechanical consequences of corrosion propagation, particularly cracking resistance.

Keywords: Limestone Calcined Clay Cement (LC^3), Reinforcement corrosion, Corrosion-induced cracking, Fracture energy, Finite element analysis

To the teachers, mentors, and loved ones who have contributed to my education, professional development, and personal growth.

Preface

The present thesis is submitted to Chalmers University of Technology in accordance with the requirements for the degree of Licentiate. The work was carried out at the Division of Structural Engineering, Department of Architecture and Civil Engineering, between September 2023 and April 2026. The research was funded by the Wallenberg Initiative Materials Science for Sustainability (WISE), financed by the Knut and Alice Wallenberg Foundation under the project entitled "Materials for the Infrastructure of Tomorrow".

Acknowledgments

First and foremost, I would like to express my deepest appreciation to my main supervisor, Prof. Karin Lundgren, and my co-supervisors, Prof. Arezou Babaahmadi and Prof. Jelke Dijkstra, for sharing their expertise, time, and dedication in advancing this research and contributing to my PhD education in the best possible way. You have shown nothing but care for my development as a researcher. The complementary nature of your team is remarkable, and it has been a pleasure to take part in the discussions that made this work possible. I look forward to continuing this journey with you. I would also like to extend my appreciation to Prof. Luping Tang for contributing his expertise and providing valuable insights for the interpretation of our experimental work. My sincere thanks also go to my PhD examiner, Prof. Minna Karstunen, for her prompt assistance with administrative formalities and for ensuring that the research work was carried out satisfactorily.

I am also very grateful to my co-workers. Thank you for fostering such a great work environment and for the pleasant conversations during coffee breaks, at lunchtime, in the laboratory, or simply across the desks. You have made this process both smooth and enjoyable. This acknowledgment also extends to former co-workers who have since moved on but who equally contributed to a pleasant work environment during their time here. Special thanks go to the staff of the Structural Engineering and Building Materials Laboratories for the excellent support provided during the experimental work.

This PhD journey would not have been possible without the unwavering support of my wife, Victoria, even when it existed only in my dreams. A large part of my gratitude belongs to you. You have been my place of comfort, where I always long to return at the end of the day. My gratitude also extends to my biological and in-law families, who, even from across an ocean, continue to inspire me to keep going.

Talles Felix
Gothenburg, April 2026

List of publications

This thesis presents a summary and an extension to the following appended paper:

[I] T. Felix, A. Babaahmadi, J. Dijkstra, and K. Lundgren, "Corrosion-induced cracking in LC^3 and OPC mortars: influence of binder type and mechanical properties", Manuscript under review, 2026.

We always refer to this publication as Paper I, according to the labeling in the list above.

In addition to the appended paper, additional research outputs produced during this doctoral project include the following contributions:

[1] T. Felix, J. Dijkstra, A. Babaahmadi, and K. Lundgren, *Long-term performance of steel-reinforced concrete with cement largely replaced by natural pozzolans*, Poster presented at the 2nd WISE Dialogue Meeting, Gothenburg, Sweden, 2024.

[2] T. Felix, A. Babaahmadi, J. Dijkstra, and K. Lundgren, *Investigating corrosion damage and characterizing corrosion in steel-reinforced low-carbon concrete*, Poster presented at the 3rd WISE Dialogue Meeting, Stockholm, Sweden, 2025.

[3] T. Felix, *Comparative Analysis of Corrosion Cracking and Mechanical Performance in LC^3 and OPC Mortars*, 5th International Conference on Calcined Clays for Sustainable Concrete, Cape Town, South Africa, 2026.

List of figures

List of tables

Abbreviations

AFm	Alumina-ferric oxide monosubstituted phase
ASTM	American Society for Testing and Materials
CMOD	Crack Mouth Opening Displacement
CO_2	Carbon dioxide
C-S-H	Calcium Silicate Hydrate
FEA	Finite Element Analysis
GP	Gypsum
H-LC^3	Higher-strength Limestone Calcined Clay Cement
H-OPC	Higher-strength Ordinary Portland Cement
ITZ	Interfacial Transition Zone
K^+	Potassium cation
LC^3	Limestone Calcined Clay Cement
LS	Limestone
L-LC^3	Lower-strength Limestone Calcined Clay Cement
L-OPC	Lower-strength Ordinary Portland Cement
MK	Metaver® K metakaolin
NaCl	Sodium Chloride
Na^+	Sodium cation
OPC	Ordinary Portland Cement
PP	PowerPozz™ metakaolin
QP	Quartz Powder
RC	Reinforced Concrete
SCM	Supplementary Cementitious Material
s/b	Sand-to-Binder
w/b	Water-to-Binder

Symbols

A_{L}	Ligament area
a	Free radial expansion of corrosion products
D_{nssm}	Non-steady-state chloride migration coefficient
E_{cm}	Young's modulus
E_{corr}	Corrosion potential
f_{c}	Compressive strength
f_{cm}	Mean compressive strength
f_{t}	Tensile strength
F	Faraday's constant
F_{S}	Splitting force
G_{F}	Fracture energy
I_{corr}	Corrosion current density
K_{corr}	Corrosion layer stiffness parameter
M	Molar mass of iron
p	Exponent controlling nonlinear corrosion-layer response
R_{p}	Polarization resistance
R^2	Coefficient of determination
r	Initial radius of reinforcing steel
t	Time
t_{crack}	Time-to-cracking
t_{n}	Interface traction
$t_{\mathrm{n}_{\mathrm{crack}}}$	Interface traction at cracking
$u_{\mathrm{n}_{\mathrm{corr}}}$	Radial deformation in the interface
$u_{\mathrm{n}_{\mathrm{corr,crack}}}$	Radial deformation in the interface at cracking
x	Corrosion penetration
$x(t)$	Corrosion penetration as a function of time
$x(t_{\mathrm{crack}})$	Corrosion penetration at cracking
z	Ionic charge number
η	Volumetric expansion coefficient
$\varepsilon_{\mathrm{corr}}$	Corrosion strain
$\varepsilon_{\mathrm{corr,crack}}$	Corrosion strain at cracking
ρ_s	Density of steel

Contents

1 Introduction

1.1 Background and motivation

The invention of Portland cement, patented in 1824 by the English mason Joseph Aspdin, revolutionized the construction sector by enabling the development of stronger and more durable structures and infrastructure. It played a key role in the expansion of housing, public buildings, and utilities, contributing to urbanization, industrialization, and economic growth throughout the nineteenth and twentieth centuries. Portland cement also enabled new design possibilities, leading to a wide range of architectural styles. Furthermore, reinforced concrete became feasible with Portland cement, paving the way for high-rise buildings and infrastructure with structural elements capable of carrying both compressive and tensile stresses. Altogether, these developments led to the mass-scale use of concrete, which is currently one of the most consumed materials worldwide, second only to water [1]. Today, the built environment relies heavily on concrete-based materials.

However, the widespread use of Portland cement poses significant environmental concerns. Cement production is the third largest source of anthropogenic carbon dioxide emissions [2], and it is highly energy-intensive. These challenges have motivated intensive research into low-carbon binder systems, where clinker is partially replaced by Supplementary Cementitious Materials (SCMs). Coal fly ash and blast furnace slag are widely used SCMs [3], but their availability is expected to decline as the energy and steel sectors decarbonize.

The potential scarcity of traditional SCMs has prompted the exploration of more abundant alternatives, such as clays and limestone. Clays are globally abundant and, after appropriate treatment, e.g., calcination, can serve as highly reactive SCMs, particularly when their mineralogical composition is favorable [3, 4]. Furthermore, calcined clays can be incorporated into ternary binder systems, where limestone has proven to be a particularly effective complementary constituent. This led to the development of Limestone Calcined Clay Cement (LC^3), which has gained recognition as a low-carbon alternative to Ordinary Portland Cement (OPC).

LC^3 can achieve reductions in CO_2 emissions of up to 40% while maintaining similar or higher strength compared to OPC. Moreover, LC^3 allows the use of low-grade materials, is globally scalable due to the widespread availability of its raw materials, requires minimal modifications to existing cement plants, does not demand additional training for practitioners, and can be cost-effective due

to reduced energy consumption and local sourcing of clays [5–7]. Furthermore, energy savings are substantial, as clays are calcined at much lower temperatures (700-850 °C) than clinker (approximately 1450 °C).

Despite these advantages, the long-term performance of emerging binder systems remains a concern. Civil engineering structures are typically designed for a service life on the order of several decades, often exceeding 50-100 years, making long-term performance assessment essential. Steel reinforcement plays a central role in ensuring structural integrity, and the corrosion of embedded steel is widely recognized as a dominant degradation mechanism in reinforced concrete infrastructure. This concern is particularly pronounced in chloride-rich environments, such as marine exposure zones or regions subjected to de-icing salts, where chloride ingress can depassivate the protective oxide layer on the steel and trigger corrosion [8]. Cementitious materials incorporating SCMs generally exhibit enhanced resistance to chloride penetration compared to OPC-based systems [9–14], with LC^3 binders showing especially favorable performance in this regard [15, 16]. Nevertheless, over sufficiently long service periods, corrosion cannot be entirely avoided. Although LC^3 has been extensively studied as a low-CO_2 alternative to OPC [5, 6, 17, 18], its behavior under corrosion-induced cracking has not yet been comprehensively investigated. The present work seeks to address this gap.

1.2 Aim and objectives

This work aims to investigate corrosion and fracture in steel-reinforced mortars produced with LC^3 and to identify the associated material properties. The performance of the LC^3 systems is benchmarked against OPC mortars. The following objectives are formulated:

1. To produce mortars incorporating OPC and LC^3 with two distinct strength classes for each binder type.

2. To investigate the corrosion level required to cause cracking in the cementitious matrix of each mortar through accelerated corrosion experiments.

3. To characterize the mortars in terms of compressive strength, tensile strength, fracture energy, and chloride transport properties.

4. To develop a finite element model of the corrosion experiment and conduct numerical analyses to support and further interpret the experimental findings.

5. To evaluate how the corrosion level required to induce cracking relates to the measured material properties.

2 Durability of reinforced LC^3 systems

2.1 Cracking and corrosion in reinforced concrete

Cracking in reinforced concrete (RC) may occur due to several factors, including restraint, temperature variations, shrinkage, creep, and structural loading [19]. According to Eurocode 2, cracking is a normal phenomenon in RC structures that should be controlled to ensure proper functionality, durability, and appearance [20]. An additional source of cracking arises from expansive chemical reactions within hardened concrete, particularly by corrosion of the steel reinforcement. The volumetric expansion associated with corrosion products causes splitting stresses acting on the concrete cover and may eventually lead to cracking. This may lead to concrete spalling, loss of serviceability, and, in severe cases, structural failure.

Corrosion is fundamentally an electrochemical process. In RC structures, four partial processes occur [21]:

1. In the steel, the anodic reaction takes place. Iron oxidizes, releasing electrons and forming iron ions:

$$\mathrm{Fe} \longrightarrow \mathrm{Fe}^{2+} + 2\,\mathrm{e}^{-}. \tag{2.1}$$

   The iron ions then undergo hydrolysis, producing acidity by releasing H^{+} ions, which locally reduce the pH:

$$\mathrm{Fe}^{2+} + 2\,\mathrm{H_2O} \longrightarrow \mathrm{Fe(OH)_2} + 2\,\mathrm{H}^{+}. \tag{2.2}$$

2. The electrons are consumed in the cathodic reaction through oxygen reduction, producing alkalinity:

$$\mathrm{O_2} + 2\,\mathrm{H_2O} + 4\,\mathrm{e}^{-} \longrightarrow 4\,\mathrm{OH}^{-}. \tag{2.3}$$

3. Electrons are transported through the steel from anodic to cathodic regions, generating an electrical current.

4. The circuit is completed by ionic transport through the pore solution, enabling current flow between anodic and cathodic regions within the concrete.

Concrete acts as a protective medium that helps maintain passivation of the steel reinforcement, thereby limiting corrosion. The period during which the steel remains passive is known as the initiation period. During this stage, the electrochemical potential at the surface of the steel and the pH of the pore solution are key factors governing passivity [22]. Aggressive agents, particularly chlorides and CO_2, progressively penetrate the cementitious matrix and eventually reach the reinforcement level. Their ingress can be accelerated by cracks caused by restraint, loading, shrinkage, creep, and other mechanisms, as well as other types of deterioration, such as freeze-thaw damage [23–26]. Such cracks may act as preferential pathways for chloride and CO_2 ingress, especially as the crack width increases [27, 28]. Once sufficient chlorides accumulate, or carbonation lowers the pH, depassivation may occur, initiating chloride-induced or carbonation-induced corrosion, respectively. At this point, the propagation period begins, during which the cross-sectional area of the steel is progressively reduced, and corrosion damage develops. In the case of chloride-induced corrosion, the degradation process is highly localized, with pitting corrosion being the predominant mechanism. This results in pronounced, localized losses of steel cross-section in the affected regions. By contrast, carbonation-induced corrosion is less localized and generally leads to a more uniform corrosion morphology, distributed over a larger surface area of the reinforcing steel.

Assuming, therefore, that chlorides or carbonation alone govern corrosion initiation may be an oversimplification, since, as indicated by Equations 2.2 and 2.3, the corrosion process can only proceed if sufficient oxygen and moisture are available. Thus, the duration of the corrosion initiation period is influenced by several interacting factors. For carbonated cementitious systems, for example, the moisture state at the steel-concrete interface plays a particularly important role, while time-varying moisture exposure conditions, pore solution chemistry, microstructure, and cover depth all govern whether carbonation-induced corrosion damage will occur [29].

2.2 Fracture in concrete and its role in corrosion damage

Like corrosion, fracture in concrete is a complex phenomenon governed by multiple interacting factors. These include the heterogeneous nature of the material, characteristic length scales, loading conditions, and environmental exposure.

Concrete is a composite material consisting primarily of aggregates, cement paste, and water. When these constituents are combined and hardened, a complex microstructure develops in which the aggregates are bonded to the surrounding paste through a porous transition region of 10-50 µm thick [30]. Crack initiation often occurs in this relatively weak interfacial zone surrounding the aggregates,

commonly referred to as the interfacial transition zone (ITZ). The ITZ forms in part due to the less efficient packing of cement grains against the aggregate surface, often described as the "wall effect" [30]. Crack propagation is then strongly influenced by aggregate size, shape, and their spatial distribution [31, 32]. Large aggregates may increase crack tortuosity and promote crack bridging, thereby enhancing energy dissipation and fracture resistance. This heterogeneity gives rise to a fracture process zone ahead of the crack tip, where microcracking, aggregate interlock, and frictional sliding occur. The existence of the fracture process zone limits the direct applicability of linear elastic fracture mechanics when structural dimensions are not large compared with its size [33].

Fracture in concrete may be characterized by tensile strength and, more fundamentally, by the post-peak tensile softening response. The stress-crack opening relationship governs how stresses are transferred as the crack widens and propagates. The area under the curve arising from this relationship defines the fracture energy, which represents the energy required to create a unit area of crack surface and is therefore a key material parameter [33, 34]. Concrete mixtures with similar tensile strengths, but different softening responses, may exhibit markedly different fracture behavior. Higher fracture energy generally delays unstable crack growth and reduces crack localization, illustrating why tensile strength alone is often insufficient to describe fracture performance [35].

One of the most important aspects of concrete fracture is the structural size. Bažant showed that the nominal strength decreases with increasing structural size due to the increasing dominance of energy release over material strength, reflecting a transition from strength-based to fracture mechanics-based behavior [35]. This size effect is associated with greater energy release capacity and greater development of the fracture process zone in larger structures. Geometry, boundary conditions, and stress gradients also influence crack initiation and stability. Notches, reinforcement detailing, and cover thickness can alter fracture behavior by modifying crack-driving forces and confinement conditions [33].

Concrete fracture is also sensitive to loading mode and loading rate. Tensile- and bending-dominated failures generally exhibit more pronounced softening behavior and fracture process zone development than compression-dominated failures. Higher loading rates often lead to an increase in apparent strength and fracture energy. However, this behavior reflects a combination of mechanisms, including changes in fracture patterns, rate-dependent processes in the cement paste (influenced by pore water), and inertial effects, making it difficult to isolate purely material rate effects [31]. Conversely, sustained or cyclic loading may reduce the effective fracture resistance through subcritical crack growth and cumulative damage, highlighting the time-dependent nature of fracture processes in concrete.

The confinement provided by reinforcement, transverse pressure, or external strengthening systems also modifies fracture behavior by restraining crack open-

ing and increasing energy dissipation. Bond action and tension-stiffening effects further couple fracture of concrete with reinforcement behavior, particularly in reinforced and prestressed concrete members [32, 36].

Environmental actions such as drying, temperature fluctuations, and chemical degradation can influence fracture both by inducing internal stresses and by modifying tensile strength, stiffness, and fracture energy [32, 33]. The distributed deterioration caused by such actions can progressively alter the fracture behavior of concrete. Although stiffness and tensile strength are often reduced, some forms of distributed damage may promote more diffuse cracking and thus increase the apparent fracture energy [37].

With regard to the corrosion-induced cracking discussed previously, damage development is governed largely by the fracture properties of the concrete rather than by the strength alone. Studies have shown that corrosion-induced cracking cannot be reliably predicted using purely strength-based criteria. Instead, fracture energy and tensile softening behavior are among the key controlling parameters [36, 38]. The formation of a fracture process zone around corrosion-induced cracks promotes gradual stress redistribution, analogous to mechanically induced cracking in other quasi-brittle materials. These considerations are particularly relevant when comparing cementitious systems with different microstructures and softening responses, since changes in fracture behavior can directly affect the corrosion level required to initiate surface cracking. Consequently, understanding the fracture properties is essential to interpret the resistance to corrosion-induced cracking.

2.3 Influence of LC^3 on corrosion behavior and fracture

When LC^3 is used instead of conventional OPC, both the microstructure and pore solution chemistry of the cementitious system are altered. A beneficial synergy exists between calcined clay and limestone through the coupling of pozzolanic reactions and carbonate-aluminate chemistry. This interaction promotes additional hydrate formation, particularly stable carboaluminate AFm phases, contributes to pore refinement, and enhances early-age hydration. Limestone supplies carbonate ions and provides nucleation sites, while calcined clay contributes reactive alumina and silica, enabling the formation and stabilization of hydrate assemblages that are not typically achieved with a single SCM [39–42].

These changes can influence corrosion behavior in both favorable and unfavorable ways. Because a substantial portion of OPC is replaced, and due to pozzolanic reaction, LC^3 systems exhibit lower alkalinity than pure OPC systems. Consequently, the passive layer formed on the steel may be less stable. Despite this, recent work reported that LC^3 exhibits a critical chloride threshold about 4.6

times higher than OPC, indicating improved resistance to chloride-induced depassivation [43]. This improvement was attributed to the formation of an AFm-rich layer on the steel surface during passivation, acting as a barrier to chloride ingress.

In addition, the combined action of limestone and calcined clay reduces chloride transport more effectively than OPC [15, 16, 44, 45]. LC^3 systems often exhibit lower permeability due to their finer particle size distribution, pozzolanic reactivity, and refined pore structure. The smaller pores create a more tortuous transport path, reducing the rate of chloride migration through the matrix [15, 17, 46, 47]. Furthermore, the hydration of LC^3 leads to dense and stable hydration products, including C-S-H and alumina-rich phases, which further improve microstructure and hinder chloride movement [45, 48, 49]. The clay-rich phases may also enhance the chloride binding capacity, thereby reducing the concentration of free chlorides available to initiate corrosion [18, 50].

On the other hand, LC^3 systems generally exhibit lower carbonation resistance because of their reduced clinker content and lower calcium hydroxide availability after hydration [5, 51, 52]. This may accelerate carbonation-induced corrosion. A recent study detected active corrosion in reinforced LC^3 concrete at an early stage of depassivation, before the carbonation front had reached the level of steel, suggesting an increased vulnerability to carbonation in high-replacement systems. In such cases, conventional service-life models assuming that propagation starts only when the carbonation front reaches the reinforcement may need reconsideration [53]. Moreover, decomposition of Friedel's salt during carbonation may release previously bound chlorides, increasing the free chloride concentration and further promoting depassivation [44].

Beyond corrosion initiation, relatively limited research has addressed LC^3 systems in the corrosion propagation stage. Nevertheless, Nguyen et al. [54] reported that reinforced LC^3 concrete exhibited corrosion potential, E_{corr}, and polarization resistance, R_{p}, trends over 500 days that were broadly comparable to those of OPC concrete under both chloride- and carbonation-induced corrosion. These findings suggest similar electrochemical behavior during propagation. Another study, in which RC specimens were subjected to ASTM G109 and impressed current corrosion tests, reported that LC^3 systems can perform better than OPC systems during the corrosion propagation phase. This behavior was primarily attributed to two factors: (i) the higher electrical resistivity of the concrete matrix, which, given that the same potential as in the OPC reference was applied during the induced current corrosion test, significantly reduced the corrosion current and, consequently, the corrosion rate; and (ii) the formation of less expansive corrosion products, which induced lower expansive stresses in the surrounding concrete [55]. It should be noted that the procedure used to treat the corrosion products prior to characterization was not specified, and their properties may have changed if they were exposed to the external environment.

However, at the time of writing, no studies were identified that explicitly ad-

dress the mechanical consequences of corrosion propagation in LC^3 systems, such as corrosion-induced crack initiation, crack propagation, or the role of rust expansion pressures. Fracture performance has likewise not been directly addressed, particularly in relation to corrosion-induced damage. Detailed investigations on the interaction between the LC^3 microstructure, fracture behavior, and stresses generated by corrosion products remain scarce. This knowledge gap provided a key motivation for the present work, which offers initial insights into fracture energy and corrosion-induced cracking in reinforced LC^3-based materials.

3 Materials and methods

The present study investigates four mortars that comprise two different binders and two strength classes governed by the 28-day compressive strength, which served as the primary performance parameter. Two mixtures were based on OPC, while the remaining two incorporated LC^3. For each type of binder, two strength levels were deliberately targeted, resulting in one higher-strength and one lower-strength variants. Accordingly, the mixtures are designated as H-OPC and L-OPC for the OPC-based mortars, and H-LC^3 and L-LC^3 for the LC^3-based mortars, where the prefixes "H-" and "L-" denote higher-strength and lower-strength, respectively.

The work was structured in three main parts. First, pilot compressive strength tests were conducted to determine the four mix designs that would constitute the H-OPC, L-OPC, H-LC^3, and L-LC^3 mortars investigated in the subsequent stages. Second, the selected mixtures were experimentally characterized with respect to their mechanical and transport properties, as well as their corrosion-induced cracking resistance. Finally, nonlinear finite element analyses were performed to further evaluate and interpret the experimental response of the materials.

The materials and methods employed in each part are described in the following sections.

3.1 Definition of materials

To select the four mortars for the main experiments, pilot compressive strength tests were conducted to evaluate the strength development of the candidate mixtures, particularly those incorporating LC^3, where the reactivity of the calcined clays required verification.

The pilot tests were performed in accordance with EN 196-1:2016 [56], where three $40 \times 40 \times 40$ mm^3 mortar prisms were tested using a MATEST E183N compression press. Eight mixtures were tested: three OPC-based and five LC^3-based. To obtain varying compressive strengths in the OPC mortars, the water-to-binder (w/b) and sand-to-binder (s/b) ratios were varied. For the LC^3 mortars, two metakaolins were tested (Metaver K® and PowerPozz™) so the strength class could be controlled by selecting the one with either higher or lower intrinsic reactivity. The gypsum content was also varied to evaluate its effect on strength development. The preparation followed the binder design proposed by Cheng et al. [57], where the calcined clays incorporated in the LC^3 mixes were produced by

blending either Metaver K® or PowerPozz™ and quartz powder at a proportion of 3:1 by weight.

The detailed composition of the pilot test mixes is given in Table 3.1.

Table 3.1: *Mixture compositions of the pilot mortar mixes.*

Mortar	Binder composition (%w)						Water-to-binder ratio	Sand[2]-to-binder ratio
	OPC[1]	MK	PP	QP	LS	GP		
OPC-a	100	0	0	0	0	0	0.5	3.125
OPC-b	100	0	0	0	0	0	0.6	3.125
OPC-c	100	0	0	0	0	0	0.6	4
MK-LC^3-a	55	22.5	0	7.5	15	0	0.5	3.125
MK-LC^3-b	52.5	22.5	0	7.5	15	2.5	0.5	3.125
MK-LC^3-c	50	22.5	0	7.5	15	5	0.5	3.125
PP-LC^3-a	55	0	22.5	7.5	15	0	0.5	3.125
PP-LC^3-b	50	0	22.5	7.5	15	5	0.5	3.125

Abbreviations: OPC = ordinary Portland cement; MK = Metaver® K metakaolin; PP = PowerPozz™ metakaolin; QP = quartz powder; LS = limestone; GP = gypsum.
[1] CEM I 52.5 R [58] was used as OPC.
[2] Crushed-stone sand with particle size ranging from 0-4 mm

The results of the pilot compressive strength tests are presented in Figure 3.1. It illustrates that, for the OPC-based mixes, the w/b ratio had a greater influence on the compressive strength than the s/b ratio. Therefore, the OPC-a and OPC-b mix designs were selected for the main tests constituting the H-OPC and L-OPC mortars, respectively.

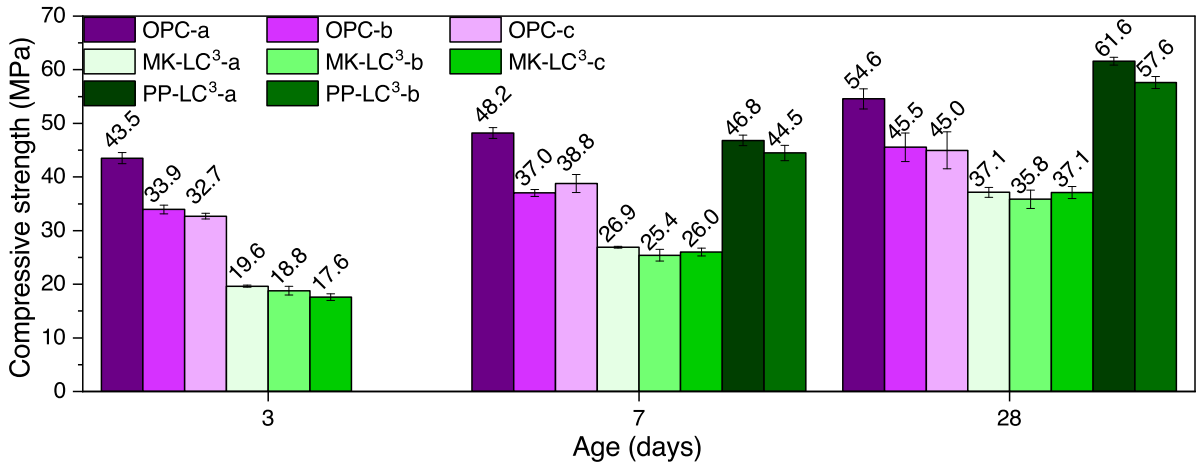

Figure 3.1: *Compressive strength development of the pilot mortar mixes.*

The LC^3-based mortars showed a large variation depending on the commercial metakaolin used. Mixtures incorporating Metaver K® showed significantly lower compressive strength compared with those incorporating PowerPozz™. The

gypsum content did not significantly affect the compressive strength. Therefore, the LC^3-based mortars containing 5% gypsum by binder weight were selected for the main tests, as this percentage resulted in compressive strengths more comparable to those of the selected OPC mixtures, as well as allowing a higher OPC replacement level. Thus, PP-LC^3-b and MK-LC^3-c were selected as the H-LC^3 and L-LC^3 mortars for the subsequent experiments.

3.2 Experimental campaign

The experimental campaign is discussed in detail in Paper I. Therefore, only a summary of the methods is presented here.

In this part of the study, corrosion of the steel reinforcement embedded in the mortars was accelerated using the impressed current technique [59, 60] to investigate the corrosion level required to induce surface cracking. This was evaluated by measuring the time t_{crack} required for cracking to occur through electrical resistance monitoring. The test consisted of four cylindrical specimens connected in series, each measuring 26 mm in diameter and 35 mm in height, with a centrally embedded 6 mm diameter reinforcing steel bar. The mortar cover was 10 mm at the sides and bottom, while the steel bar protruded above the top surface to allow cable connection. A schematic illustration of the geometry of the specimen is presented in Figure 1 of Paper I. In the electrical setup, the reinforcing steel acted as the cathode and a copper mesh surrounding the specimens functioned as the anode. The setup was immersed in a 5% NaCl aqueous solution, which provided the electrolyte for the electrical circuit. A constant current density of $I_{\text{corr}} = 50\ \mu\text{A}\,\text{cm}^{-2}$, which is considered appropriate for accelerated corrosion experiments [61], was applied. The corrosion test setup is illustrated in Figure 2 of Paper I.

In parallel, complementary experiments were conducted to determine the mechanical and transport properties of the mortars after 28 days of curing, enabling a more comprehensive interpretation of the corrosion behavior.

The compressive strength f_{c} of the selected mortars was first determined by uniaxial compression tests performed according to EN 12390-3 [62] on $100 \times 100 \times 100$ mm^3 cubes. The compressive strength was measured at this larger specimen scale in order to better account for structural level behavior and reduce potential size effects.

In addition, wedge-splitting tests were conducted following the methodology proposed by Brühwiler [63]. In this test, $100 \times 100 \times 100$ mm^3 cubic specimens with a groove and a notch were subjected to splitting loading while the splitting force F_{S} and the crack mouth opening displacement (CMOD) were recorded. With the experimental data, the tensile strength f_{t} of the mortars was calculated, and the fracture energy G_{F} was determined by integrating the F_{S}-CMOD curve and normalizing the resulting area by the ligament area A_{L} of the specimens. This

parameter represents the energy dissipated per unit area of the fractured surface.

Finally, the resistance to chloride transport was assessed by measuring the chloride migration coefficient D_{nssm} using the non-steady-state migration method NT BUILD 492 [64]. In this method, water-saturated specimens are subjected to an externally applied electrical potential that accelerates the migration of chloride ions from a NaCl solution into the material. After the prescribed test duration, the specimens are split, and the chloride penetration depth is determined by spraying the fracture surface with a silver nitrate solution, which produces a visible color change in the presence of chlorides. The penetration depth is measured at several locations and averaged, and D_{nssm} is subsequently calculated according to the formulation presented in [64].

Ultimately, to evaluate how the corrosion level required to induce cracking is related to the measured material properties, the latter were analyzed in relation to the observed t_{crack} values.

3.3 Finite element model and analysis

To further interpret the experimental observations and investigate the mechanisms governing corrosion-induced cracking, the corrosion experiment was reproduced in finite element analyses. Based on the specimen geometry and the mechanical properties measured experimentally, a numerical model was developed using DIANA FEA, version 10.10 [65]. The numerical model and analysis procedures are described in the following sections.

Model geometry

The geometry of the model represents a short cylindrical mortar specimen with a centrally embedded reinforcing steel bar, reproducing the specimens used in the corrosion experiments. The reinforcing bar was modeled with solid elements. Instead of a perfectly circular cross-section, the bar was approximated by a 12-sided polygon, which provides an accurate representation of a circular bar while facilitating structured meshing. The polygon was extruded along the longitudinal direction to form a steel bar with a diameter of 6 mm and an embedded length of 25 mm inside the mortar. In addition, a 10 mm segment that protruded above the mortar surface was included to represent the portion where the electrical cables were connected during the corrosion tests.

The mortar specimen was modeled as a cylindrical body with a radius equal to the sum of the steel radius and the mortar cover, resulting in a radius of 13 mm. The specimen height was 35 mm. The steel geometry was subtracted from the mortar cylinder, creating a cavity that represents the location of the reinforcement and ensuring that the steel and mortar were represented as separate solid domains. In addition, the specimen was assumed to rest on a 5 mm thick supporting plate,

which was modeled with sheet elements. The plate had the same radius as the mortar specimen and represents the bottom of the plastic container used in the experimental setup. Interface elements were placed between the plate and the mortar cylinder to simulate contact, as described below in Boundary conditions. The model geometry is illustrated in Figure 3.2.

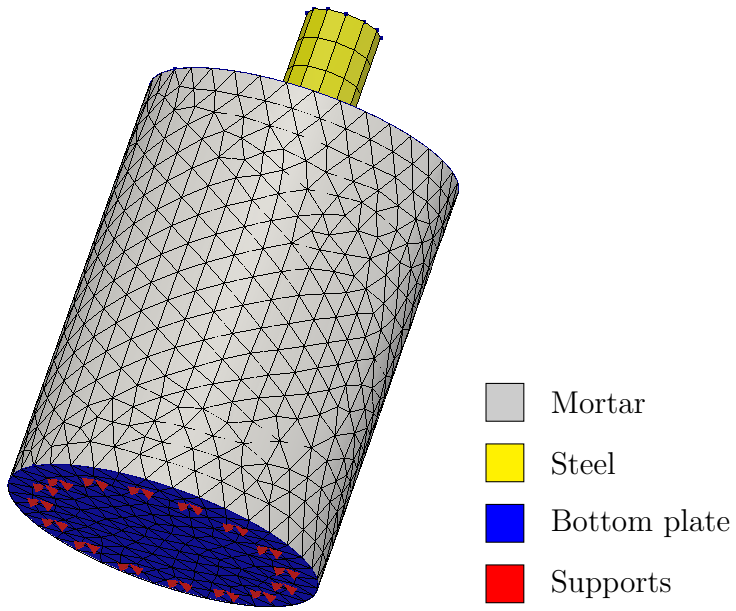

Figure 3.2: *Finite element model used in the numerical analysis. The figure shows the mortar specimen, the protruding part of the embedded reinforcing steel bar, bottom support plate, applied boundary conditions, and the finite element mesh. The boundary conditions were applied over the entire lower surface of the support plate; their graphical representation is simplified for clarity.*

A key aspect of the model is the representation of the steel-mortar interface, where corrosion-induced expansion occurs. This interface was discretized using specialized interface elements placed between the steel and mortar surfaces. Because the reinforcement cross-section is represented as a 12-sided polygon, the interface is divided into twelve segments, each corresponding to one side of the polygon. These interface elements allow relative displacement between the steel and the surrounding mortar and incorporate expansion effects that simulate the volumetric increase associated with the formation of rust. The expansion was implemented through a user-defined interface routine described below in Corrosion model. Additional interface elements were placed at the bottom of the bar with the same properties as the other elements, but without corrosion expansion in order to avoid unrealistic stress concentrations at that location.

Mesh

As illustrated in Figure 3.2, the finite element mesh was generated using different first-order element types for each material domain to balance accuracy and computational efficiency.

The reinforcing steel bar was meshed with 8-node brick, 5-node pyramid, 3-sided 4-node tetrahedron, and 6-node wedge elements, which ensured alignment between the geometry of the polygonal bar and the interface elements placed around its perimeter. The mesh around the steel bar was structured so that each polygon side corresponded to one interface segment, ensuring compatibility between the interface elements and the surrounding solid elements.

For the mortar cylinder, the mesh was generated using 3-sided 4-node tetrahedron elements. This mesh type allowed for more flexible discretization of the curved cylindrical geometry and facilitated a robust mesh transition around the steel-mortar interface. Tetrahedral elements were also preferred for the mortar because their unstructured meshing pattern allows a more natural representation of crack development, enabling diagonal, irregular, or otherwise non-prescribed cracking paths to be captured more realistically.

Finally, for the supporting plate, 3-node triangular elements were used, whereas for the mortar cylinder-steel and mortar cylinder-supporting plate interfaces, 3+3-nodes 3-D plane triangular elements were used.

Boundary conditions

To represent a compliant contact layer between the mortar cylinder and the supporting plate, a small stiffness (1000 MPa) was assigned to the mortar-plate interface in the normal and shear directions. It reflects the fact that, in reality, the specimen rests on a plate with surface roughness and slight deformability rather than being perfectly bonded or rigidly supported. Numerically, this behaves as a distributed spring support, preventing unrealistic stress concentrations that would occur with a fully rigid boundary condition.

Boundary conditions were applied to the plate by constraining translational degrees of freedom to all nodes in all directions. This configuration approximates a specimen resting on a rigid base with low stiffness spring supports.

Material models

The steel reinforcement was modeled as a linear elastic material with a Young's modulus of 200 GPa and a Poisson's ratio of 0.3.

The mortar was modeled using a total strain crack model [65]. The material behavior was defined as linear elastic prior to cracking, with a Poisson's ratio of 0.2. The Young's modulus E_{cm} was defined according to Eurocode 2 (EN 1992-1-

1) as

$$E_{\mathrm{cm}}[\mathrm{GPa}] = 22\left(\frac{f_{\mathrm{cm}}[\mathrm{MPa}]}{10}\right)^{0.3}, \tag{3.1}$$

where f_{cm} is the mean compressive strength of the mortar [20].

The tensile behavior was described using the Hordijk softening curve [66], which provides a nonlinear stress-crack opening relationship calibrated for fracture mechanics-based analyses. The experimentally determined tensile strength and fracture energy were used as input to ensure consistency with the properties of the tested mortars. The smeared crack approach was applied, assuming localization to take place within a single element band. The crack bandwidth was defined according to Rots' formulation, in which it is determined by the element size, type, and interpolation function [65]. A rotating crack formulation was adopted, allowing the crack orientation to evolve with the principal strain directions during loading. The validity of these assumptions was verified by comparison with principal strain contour plots, see Figure 4.2.

In compression, the mortar followed the Thorenfeldt constitutive model [67], which captures the nonlinear descending branch beyond the peak stress. The compressive strength was also set according to the mean value obtained from the uniaxial compression tests.

Corrosion model

The corrosion model used in the simulations is based on the formulation proposed by Lundgren [36] and adapted by Alhede [68]. In this approach, a radial expansion occurs at the steel-mortar interface, representing the volumetric growth of corrosion products.

In this model, the corrosion penetration x at each time step is computed from the experimentally imposed corrosion current density $I_{\mathrm{corr}} = 50\ \mu\mathrm{A\,cm^{-2}}$ using Faraday's law, expressed as

$$x\,(t) = \frac{I_{\mathrm{corr}} M}{zF\rho_s} t, \tag{3.2}$$

where M is the molar mass of iron, z is the ionic charge number, F is Faraday's constant, ρ_s is the density of steel, and t is time. In essence, $x\,(t)$ represents the thickness of steel consumed during the corrosion process at a given time. For simplicity, corrosion was assumed to progress uniformly along both the length and the perimeter of the reinforcing bar in the present analyses. Therefore, $x\,(t)$ increases at the same rate over the entire surface of the steel-mortar interface.

Because corrosion products occupy a larger volume than the original steel, this penetration is converted into a radial rust expansion. The free radial expansion a of the corrosion layer is expressed as

$$a = -r + \sqrt{r^2 + (\eta - 1)\,(2rx - x^2)}, \tag{3.3}$$

where r is the initial radius of steel and η is the volumetric expansion coefficient, defined as the ratio between the volume of rust and the uncorroded steel. In the simulations presented here, a constant $\eta = 4$ was assumed. This value represents a reasonable approximation based on experimentally measured volumetric expansion coefficients reported in earlier research for similar specimens corroded under comparable conditions [69–71].

The mechanical behavior of the corrosion layer is described by the corrosion strain $\varepsilon_{\text{corr}}$, defined as

$$\varepsilon_{\text{corr}} = \frac{u_{\text{n}_{\text{corr}}} - a}{x + a}, \tag{3.4}$$

where $u_{\text{n}_{\text{corr}}}$ is the radial deformation in the interface.

When the corrosion products are confined by the surrounding mortar, compressive stress develops in the corrosion layer. This stress is transmitted to the mortar through the interface elements and is calculated using a nonlinear stress-strain relationship between the interface traction t_{n} and $\varepsilon_{\text{corr}}$ as

$$t_{\text{n}} = K_{\text{corr}} \varepsilon_{\text{corr}}^{p}, \tag{3.5}$$

where K_{corr} is a stiffness parameter and p is an exponent controlling the nonlinear response.

Following Lundgren [36], these parameters were established by back-calculating the mechanical response of the corrosion layer from published corrosion-cracking experiments, see [72–75], in which the corrosion penetration at cracking $x\,(t_{\text{crack}})$ had been evaluated. In that procedure, the corrosion penetration required to crack the mortar cover was combined with finite element analyses of the corresponding specimen geometries to determine the normal stress and deformation of the corrosion layer at cracking, $t_{\text{n}_{\text{crack}}}$ and $u_{\text{n}_{\text{corr,crack}}}$, respectively. These values were then substituted into Equations 3.3 and 3.4 to determine the corrosion strain at cracking, $\varepsilon_{\text{corr,crack}}$. The results, together with selected specimen parameters from the cited experimental studies, are summarized in Table 3.2. This procedure allowed individual stress-strain data points for the corrosion products to be constructed and subsequently fitted by the above power-law relation. The resulting calibration indicated that the corrosion products behave similarly to a granular material, exhibiting low initial stiffness but pronounced stiffening under increasing confinement.

Although Lundgren's original calibration was developed for a lower volumetric expansion coefficient ($\eta = 2$), the same constitutive framework was applied here together with $\eta = 4$, following Alhede's adaptation [68]. This affects the free radial expansion a and, consequently, the resulting corrosion strain $\varepsilon_{\text{corr}}$ evolution. Accordingly, new calibrated values for the model were obtained; $K_{\text{corr}} = 0.9$ GPa and $p = 11$ were adopted in the present work. The resulting curve, together with the individual stress-strain data points, is shown in Figure 3.3.

Table 3.2: *Experimental and numerically evaluated parameters used to determine the corrosion strain at cracking for a volumetric expansion coefficient $\eta = 4$.*

Reference	Test number	r (mm)	$x\,(t_{\mathrm{crack}})$ (µm)	$t_{\mathrm{n_{crack}}}$ (MPa)	$u_{\mathrm{n_{corr,crack}}}$ (µm)	a	$\varepsilon_{\mathrm{corr,crack}}$
Ghandehari et al. [72]	CsRs	5	159	-22.2	15.1	0.45	-0.71
	CIR1	10	92	-14.3	15.6	0.27	-0.69
	CsR1	10	72	-9.8	9.66	0.21	-0.70
Cabrera and	opc	6	68	-25.8	21.4	0.20	-0.65
Ghoddoussi [73]	pfa	6	192	-25.8	21.4	0.54	-0.70
Al-Sulaimani et al. [74]	5	8	115	-24.5	20.6	0.33	-0.68
	7	8	102	-17.3	17.3	0.30	-0.69
	10	8	93	-11.8	14.3	0.27	-0.69
Andrade et al. [75]	I	8	17.9	-6.83	4.2	0.05	-0.63
	II	8	14.4	-7.5	4.39	0.04	-0.59
	III	8	21.3	-10.8	6.8	0.06	-0.63
	IV	8	17.4	-7.5	4.39	0.05	-0.63

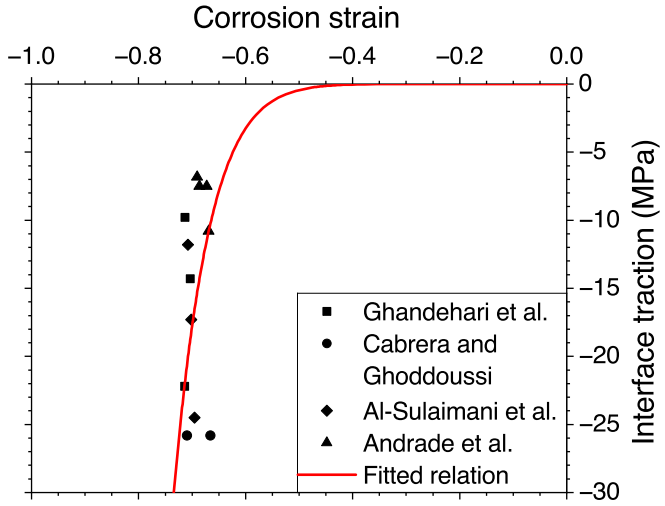

Figure 3.3: *Normal stress versus corrosion strain at cracking data points obtained from a combination of numerical [36] and experimental results (Ghandehari et al. [72], Cabrera and Ghoddoussi [73], Al-Sulaimani et al. [74], and Andrade et al. [75]). The interface traction-corrosion strain relationship was fitted for a volumetric expansion coefficient $\eta = 4$, resulting in a stiffness parameter $K_{\mathrm{corr}} = 0.9$ GPa and an exponent $p = 11$ in the relation $t_{\mathrm{n}} = K_{\mathrm{corr}}\varepsilon_{\mathrm{corr}}^{p}$.*

Nonlinear analysis

The numerical simulation was performed as a nonlinear incremental analysis in which the corrosion penetration was gradually introduced and the mechanical response of the system was solved at each increment. The analysis was defined as a nonlinear execution block, allowing the model to capture material nonlineari-

ties such as cracking in the mortar and the nonlinear response of the corrosion interface.

The corrosion process was simulated through several incremental time steps by implementing the corrosion model described above through a user-defined interface routine. The time steps were defined so that the simulation time corresponded to the duration of the corrosion experiments for the four mortars studied in this work.

At each increment, the corrosion model updates the corrosion penetration and the associated free expansion of corrosion products, which generates pressure at the steel-mortar interface and induces stresses in the surrounding mortar. The actual expansion is found from equilibrium at every increment, which is solved using the Newton-Raphson iterative method. Convergence of the iterative solution was monitored using three independent criteria based on force residuals, displacement increments, and energy balance. Once one of these criteria was satisfied, the iteration was considered converged, and the analysis proceeded to the next increment.

3.4 Research overview

To provide a clear overview of the experimental and numerical program, the complete research workflow is summarized in Figure 3.4. This diagram presents the logical progression of the study from the research questions to the corresponding objectives, approaches, and outputs. It also illustrates how the different parts of the methodology are connected, as well as how each step contributes to addressing the overall aim of the thesis.

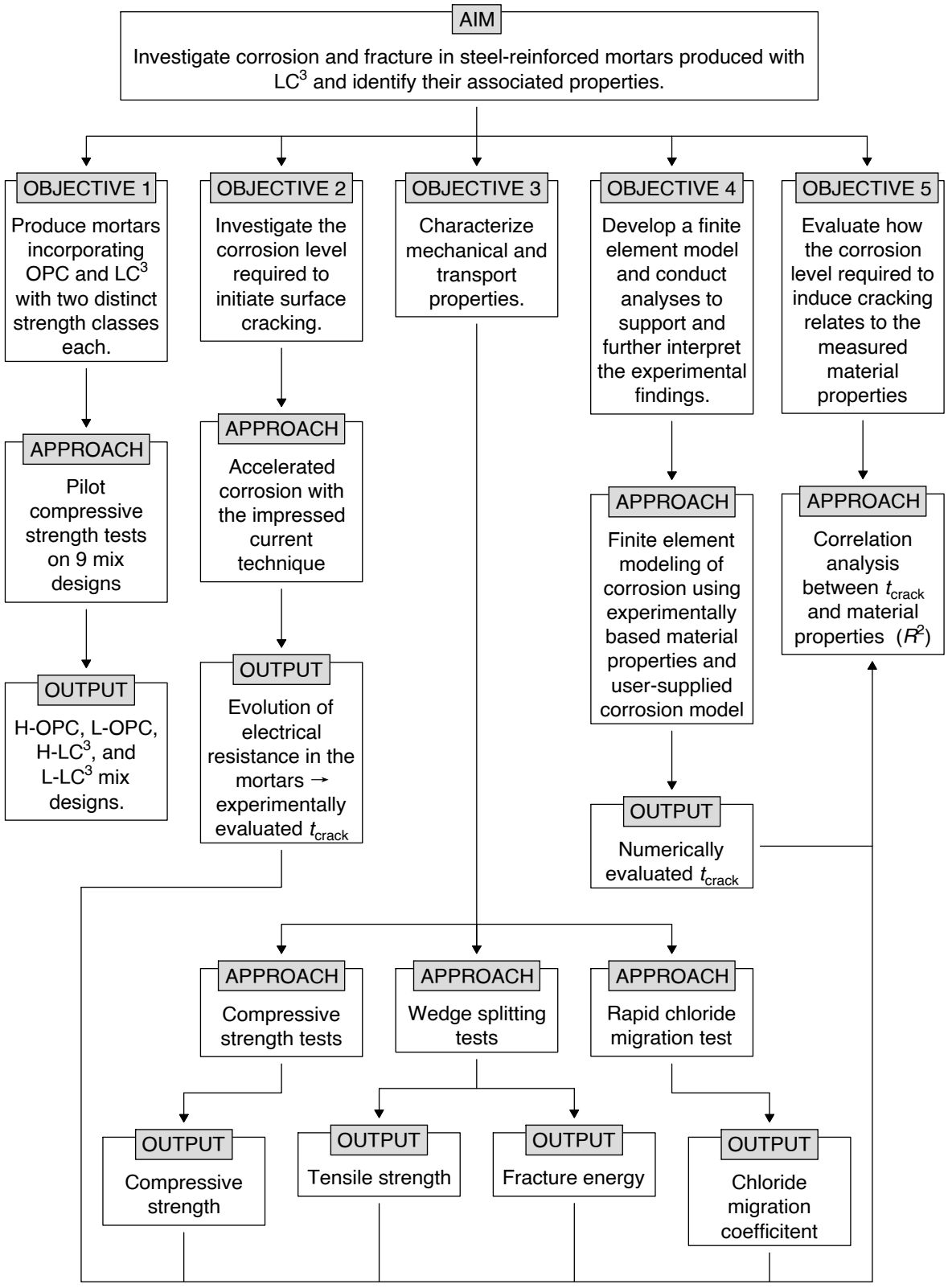

Figure 3.4: *Overview of the research, linking the aim, objectives, methodological approaches, and resulting outputs.*

4 Summary of results

This chapter presents the main results of the study, including a summary of the mechanical, transport, and corrosion-induced cracking resistance properties of the H-OPC, L-OPC, H-LC^3, and L-LC^3 mortars, which are discussed in greater detail in Paper I.

The chapter is organized into three sections. The first summarizes the mechanical and transport properties of the mortar systems. The second reports their resistance to corrosion-induced cracking and the relation between the cracking behavior and the material properties. The final section presents the results of the nonlinear finite element analysis and compares them with the experimental observations.

4.1 Material properties

The mechanical and transport properties of the selected mortars were evaluated after 28 days of curing to characterize the influence of the binder composition on material performance. The investigated properties included compressive strength f_c, tensile strength f_t, fracture energy G_F, and chloride migration coefficient D_{nssm}. These are summarized in Table 4.1.

Table 4.1: *Physical, mechanical, and transport properties of the mortars after 28 days of curing. Values represent the mean ± standard deviation of three specimens, unless otherwise stated.*

Mortar	Density ($g\,cm^{-3}$)	f_c (MPa)	f_t (MPa)	G_F ($N\,m^{-1}$)	D_{nssm} ($\times 10^{-12}\ m^2\,s^{-1}$)
H-OPC	2.24 ± 0.05	63.1 ± 2.4	4.19 ± 0.01	91.4 ± 1.7	16.1 ± 2.2
L-OPC	2.20	49.8	4.11 ± 0.10	85.2 ± 3.2	14.9 ± 0.3
H-LC^3	2.20 ± 0.00	66.9 ± 0.5	4.32 ± 0.01	$< 69.0 \pm 4.3$[1]	1.9 ± 0.8
L-LC^3	2.19 ± 0.02	40.2 ± 0.3	3.40 ± 0.15	47.7 ± 2.5	8.1 ± 0.3

[1] The brittle post-peak response of the H-LC^3 mortars in the wedge-splitting test caused an abrupt force drop that was difficult to track under displacement control. The reported G_F value is therefore likely overestimated and should be interpreted as an upper bound.

The higher-strength mortars exhibited comparable compressive strengths, with H-LC^3 slightly outperforming H-OPC. These results are consistent with previous

findings for LC^3 containing similar kaolinite levels [18, 48]. Among the lower-strength mixtures, compressive strengths ranged between 40-50 MPa, with L-LC^3 presenting the lowest value. These results confirm the intended separation between strength classes.

The tensile strength varied only modestly between H-OPC, L-OPC, and H-LC^3. In contrast, L-LC^3 showed a distinctly lower tensile capacity, indicating that the reactivity of the calcined clay influenced the tensile response.

The differences in the fracture performance were more pronounced. The wedge-splitting tests showed that the LC^3 mixtures exhibited a more brittle post-peak behavior than the OPC mortars. In particular, H-LC^3 experienced a sudden force drop (see Figure 5 in Paper I), which limited reliable capture of its post-peak curve and likely resulted in an overestimation of G_F. Overall, LC^3 mixtures displayed significantly lower fracture energies, highlighting that fracture behavior is strongly dependent on the type of binder.

The transport performance showed the opposite trend. Both LC^3 mortars exhibited substantially lower D_{nssm} values than the OPC mixtures. The migration coefficient of H-LC^3 was nearly an order of magnitude lower than that of the OPC mortars, consistent with previous research [16]. These results demonstrate the strong beneficial impact of LC^3 on resistance to chloride ingress.

Overall, the LC^3 mortars combined enhanced resistance to chloride transport with a more brittle fracture response compared with the OPC systems.

4.2 Corrosion test

Corrosion-induced cracking was assessed using an impressed-current corrosion test. The time-to-cracking t_{crack} was determined from the moment a distinct drop in electrical resistance occurred. The electrical resistance profiles of all specimens are shown in Figure 6 of Paper I. The resulting t_{crack} values are presented in Figure 4.1.

The OPC mortars required longer corrosion exposure before cracking. Both LC^3 mixtures cracked earlier, indicating that surface cracking occurred at lower corrosion levels in the LC^3 systems.

It should be noted, however, that the lower pore solution alkalinity associated with LC^3 systems may reduce the stability of the passive film on embedded steel compared with OPC systems. In more alkaline OPC systems, oxygen evolution reactions may dominate for longer periods before the onset of active steel dissolution. As a result, depassivation and the onset of active corrosion could occur earlier under impressed-current conditions, meaning that direct comparisons of time-to-cracking based solely on Faraday's law may underestimate differences in the actual corrosion state between binders. To examine this effect, the early evolution of the electric potential of the specimens was analyzed. An initial period of relatively stable potential was followed by a marked increase, which may in-

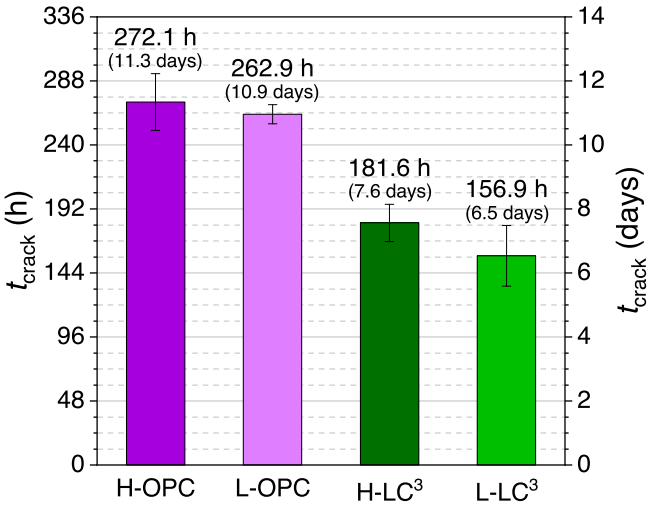

Figure 4.1: *Estimated time-to-cracking, t_{crack}, of the mortars subjected to reinforcement corrosion.*

dicate a transition from predominantly oxygen evolution and passive behavior to increasing active corrosion after partial breakdown of the passive layer. Even after corrosion initiation, some parallel oxygen evolution may still occur in steel areas that remain passive. The subsequent increase in potential was likely influenced by the accumulation of corrosion products, which can partially block pore pathways and increase local resistance. This initial stage appeared to be longer for H-OPC than for H-LC^3, while it was shorter for both low-strength mortars. However, since the duration of this transient period was small compared with the total test duration, less than 20 hours in all cases, its influence on the final time-to-cracking results is expected to be limited.

Clear differences were also observed in the evolution of electrical resistance (see Figure 6 in Paper I). The LC^3 mortars exhibited higher initial resistance, consistent with their refined pore structure and lower ionic conductivity. In H-LC^3, a temporary increase followed by a gradual decrease was observed. This behavior may be attributed to the imposed current density locally exceeding the ionic transport capacity of the low-permeability mortar. Under such conditions, ions from the external electrolyte cannot migrate rapidly enough through the pore network to maintain charge balance at the steel surface. Therefore, the region near the steel initially relies on the alkaline pore solution already present in the mortar, where hydroxyl ions and alkali cations (K^+, Na^+) help maintain ionic conductivity and electroneutrality. As these readily available ions are depleted, portlandite begins to dissolve in order to buffer the pore solution alkalinity. As the affected zone expands outward from the steel, the measured resistance gradually increases. The resistance reaches a maximum when corrosion-induced microcracking improves local transport pathways, after which it gradually decreases until the mortar cover is fully cracked.

To examine the relationship between material properties and cracking resistance, the t_{crack} values were correlated with the measured properties. The plots are displayed in Figure 9 of Paper I, and the resulting coefficients of determination are summarized in Table 4.2.

Table 4.2: *Coefficients of determination, R^2, between t_{crack} and selected material properties.*

Property	R^2
Compressive strength	0.1005
Tensile strength	0.3159
Fracture energy	0.9149
Chloride migration coefficient	0.7129

The compressive strength did not show a significant correlation with t_{crack}. The tensile strength showed only a weak correlation. In contrast, the fracture energy exhibited a very strong linear relationship, demonstrating that materials with higher fracture energy required higher corrosion levels to crack. Furthermore, considering that the fracture energy of H-LC^3 was likely overestimated due to its brittle behavior in the wedge-splitting test, as discussed in Section 4.1, an even higher coefficient of determination could be expected if the post-peak response had been captured more reliably. This strong correlation indicates that corrosion-induced cracking is fundamentally governed by energy dissipation capacity rather than strength, supporting a fracture-mechanics-based interpretation of durability. Finally, the chloride migration coefficient showed a moderate correlation, suggesting that while transport properties are relevant to durability, they are not the primary factor that governs cracking in the propagation stage.

In general, the results indicate that fracture-related parameters, particularly fracture energy, are more influential in governing corrosion-induced cracking than conventional strength or transport indicators.

4.3 Nonlinear finite element analyses

To further interpret the experimental findings, finite element models were developed using the measured material properties as input.

The time-to-cracking, t_{crack}, was evaluated by monitoring the evolution of strain at the mortar surface. For each type of mortar, the surface element that exhibited the highest tensile strains was identified, as exemplified in Figure 4.2, and the corresponding strain-time curve from one of its nodes was extracted. Cracking was assumed to initiate when a sharp increase in strain occurred. To identify this point objectively, the second derivative of the strain-time curve was computed in OriginPro® [76], and the time corresponding to the peak of this curve was taken

as t_{crack}. The resulting strain-time curves are shown in Figure 4.3. The numerical values of t_{crack} are compared with the experimental results in Table 4.3. Both experimental and numerical values were normalized with respect to H-OPC.

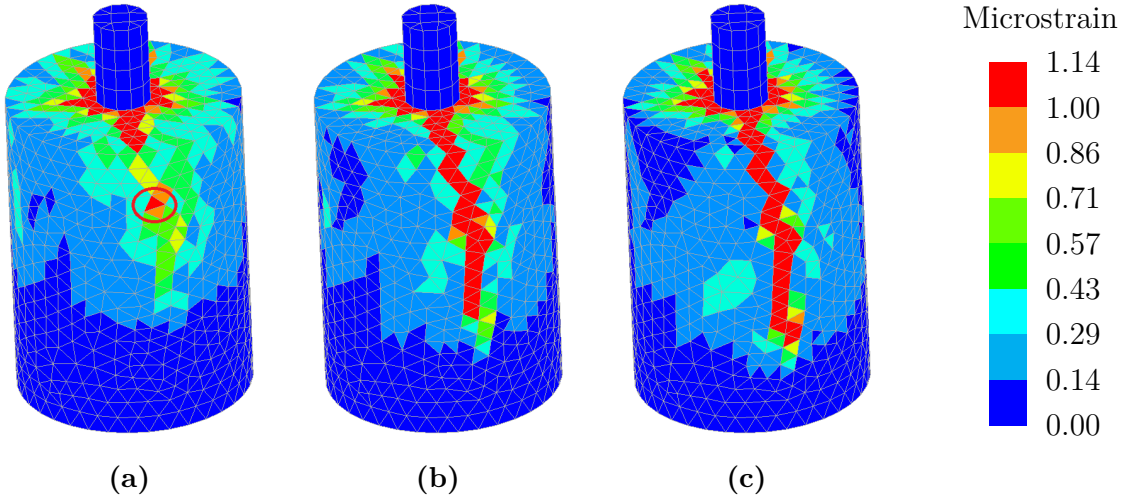

Figure 4.2: *Cracking development in the FEA of the H-OPC specimen: (a) right before cracking (t = 333.3 h), with the element exhibiting the highest tensile strain highlighted; (b) at t_{crack} = 340.3 h; (c) after cracking (t = 375.0 h).*

Table 4.3: *Experimental and numerical time-to-cracking, variation between them, and values normalized with respect to H-OPC.*

Mortar	t_{crack} (h)		Variation	Normalized to H-OPC	
	Experiment	FEA		Experiment	FEA
H-OPC	272.1	340.3	25%	1.00	1.00
L-OPC	262.9	326.4	24%	0.97	0.96
H-LC^3	181.6	273.6	51%	0.67	0.80
L-LC^3	156.9	197.2	26%	0.58	0.58

In all cases, the numerical model predicted later cracking than observed experimentally. These discrepancies likely arise from simplifications in the model, including the assumption of uniform corrosion along the reinforcing bar. Uniform corrosion distributes radial stresses more evenly, potentially delaying cracking relative to the more localized stress development from localized corrosion observed experimentally. Also, in the FEA, the calibration of the corrosion model with a volumetric expansion coefficient of $\eta = 4$ should be further evaluated, since the original calibration was developed using $\eta = 2$ [36].

When t_{crack} was normalized to H-OPC, there was a good agreement between simulations and experiments for L-OPC and L-LC^3. This suggests that, even though the model predicted later cracking in absolute terms, it was still able to

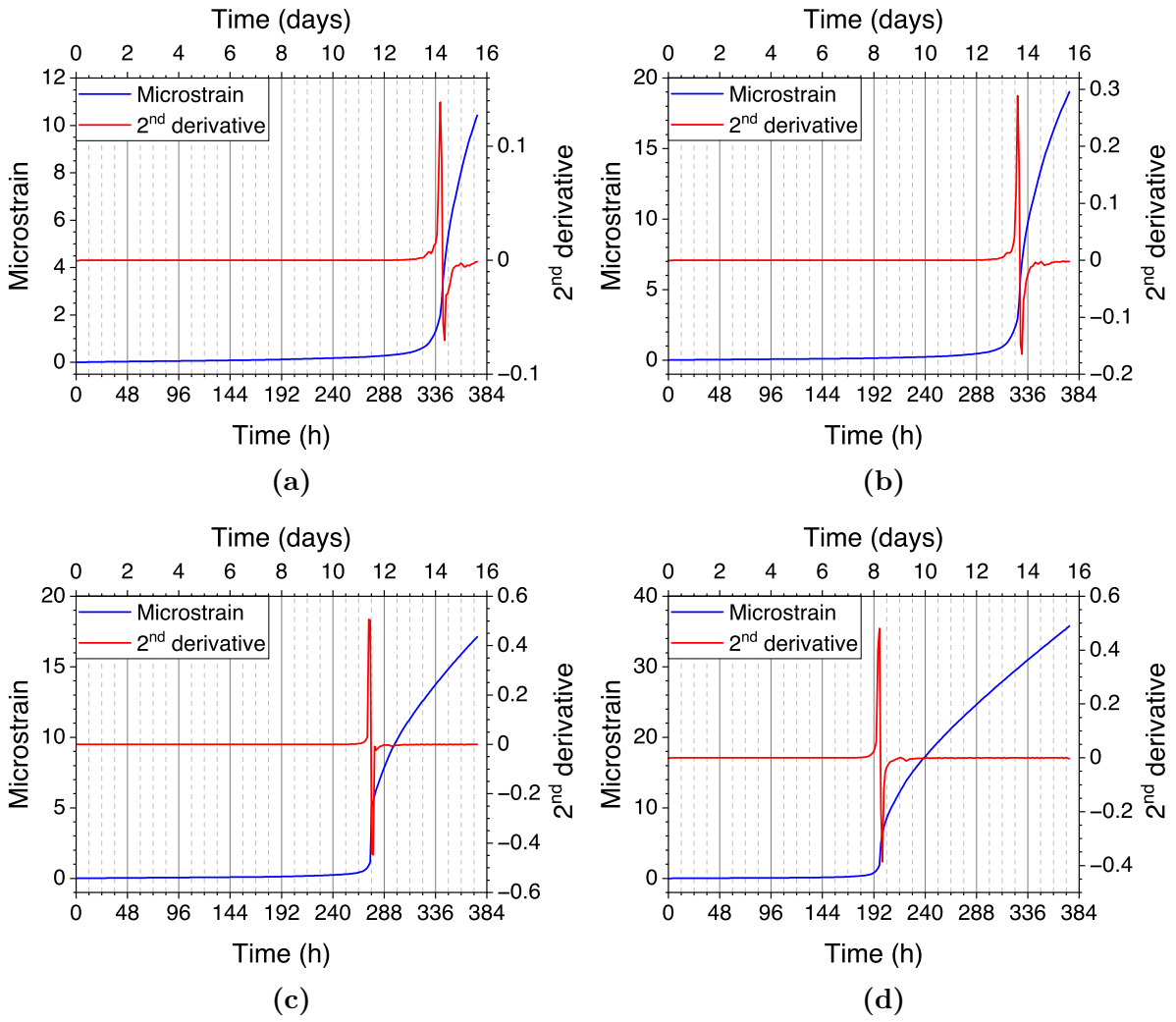

Figure 4.3: *Strain-time curves from the surface element exhibiting the largest tensile strains on the (a) H-OPC, (b) L-OPC, (c) H-LC³, and (d) L-LC³ mortars. The blue curves show the evolution of microstrain over time, while the red curves represent the corresponding second derivative of strain with respect to time.*

capture the relative differences between most mixtures. Therefore, if the calibration of the corrosion model is improved, the numerical results would likely show a better overall agreement with the experiments. The main exception was H-LC^3, which exhibited a substantially larger discrepancy: experimentally, it cracked at 67% of the H-OPC time, whereas numerically it cracked at 80%. This deviation may be attributed to the overestimated fracture energy of H-LC^3 (see Section 4.1) and to microstructural differences not explicitly modeled.

The numerical analysis also confirmed the strong relationship between the fracture energy and t_{crack}. As shown in Figure 4.4, the coefficient of determination R^2 was close to 1, consistent with the experimental observations. This highlights that fracture-related properties are key in describing damage development caused

by expansive stresses induced by corrosion.

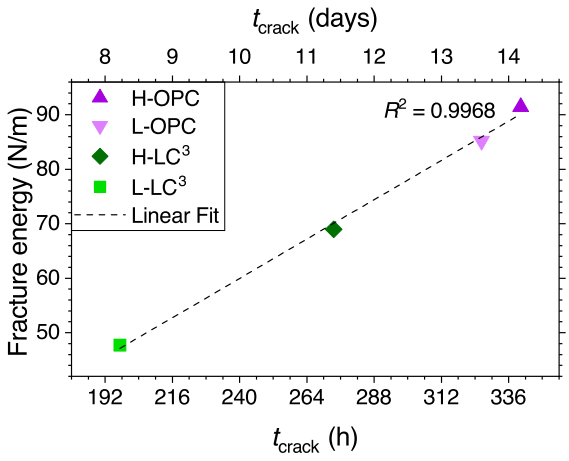

Figure 4.4: *Correlation between fracture energy and time-to-cracking,* t_{crack}*, obtained from the finite element analyses.*

5 Conclusions

This study investigated the resistance of steel-reinforced LC^3 mortars to corrosion-induced cracking and compared their behavior with that of OPC mortars. Different strength levels were considered to assess whether LC^3 systems respond differently to expansive stresses caused by corrosion products and whether this behavior can be predicted from measurable material properties. The work included the selection of mix designs, experimental characterization of mechanical, transport, and corrosion-related properties, as well as nonlinear finite element analyses of the corrosion tests using the measured properties. The main findings of the study and recommendations for future research are presented in the following sections.

5.1 Key findings

- Two distinct strength classes for both OPC and LC^3 mortars were achieved during the materials definition phase of this study. For the OPC mortars, the water-to-binder ratio had a stronger influence on compressive strength than the sand-to-binder ratio. For the LC^3 mortars, the compressive strength depended strongly on the type of commercial metakaolin used, while the gypsum content had only a limited effect.

- Surface cracking occurred at lower corrosion levels in the LC^3 mortars compared with OPC mortars during the current-induced corrosion test. This indicates that LC^3 mortars have lower resistance to corrosion-induced cracking.

- The wedge-splitting test showed a clear variation in fracture performance between LC^3 and OPC mortars designed for comparable strength levels. The LC^3 mortars exhibited a more brittle fracture response than that of OPC mortars, particularly in the H-LC^3 system, despite showing comparable compressive and tensile strengths. As a consequence, significantly lower fracture energy values were observed. This demonstrates that optimizing binder design based solely on compressive strength should be reconsidered.

- Through the rapid chloride migration test, the substantial resistance of the LC^3 systems against chloride transport was evidenced, corroborating previous research.

- Nonlinear finite element analyses showed that the measured material properties were generally able to reproduce the relative cracking behavior of the different mortars under corrosion-induced expansion. Although the model consistently predicted later cracking than observed experimentally, it captured the ranking of most mixtures when results were normalized, indicating that the overall modeling approach is valid but requires improved calibration of the assumptions for corrosion expansion.

- A strong correlation was observed between the fracture energy and the corrosion level required to induce surface cracking, both in the experiments and the numerical analyses. This shows that the fracture energy is a key parameter that governs the development of damage during the propagation stage of corrosion-induced deterioration.

- The results highlight a potential trade-off in the long-term durability performance of steel-reinforced LC^3 systems when compared with conventional OPC-based materials. On the one hand, the LC^3 binders provide significantly improved resistance to chloride ingress, contributing to a delay in the onset of chloride-induced corrosion. On the other hand, once corrosion is initiated, the surrounding cementitious matrix has a reduced capacity to accommodate the internal stresses generated by the volumetric expansion of corrosion products. These observations emphasize the importance of considering not only transport-related properties but also fracture-related parameters when evaluating the durability performance of alternative binder systems.

5.2 Outlook

The high resistance of the LC^3 systems to chloride ingress may be partially compromised by cracking that inevitably occurs in concrete structures due to mechanisms such as restraint, mechanical loading, freeze-thaw cycles, shrinkage, and creep. Such cracks act as preferential pathways for chloride transport [19, 77, 78], thereby shortening the corrosion initiation phase and, when combined with the lower resistance to corrosion-induced cracking observed in this study, may lead to earlier visible corrosion damage. A natural continuation of the present work is therefore to quantify chloride transport and corrosion initiation in pre-cracked LC^3 concrete with different crack widths and crack patterns.

It should also be noted that the experimental program was limited to mortar-scale specimens and a curing period of 28 days. In concrete systems, the aggregate size and distribution may influence fracture behavior. Previous research has shown that SCMs can strengthen the interfacial transition zone (ITZ) [79], potentially altering the preferred crack propagation path from the paste-aggregate interface to propagation through the aggregates themselves. Furthermore, the relatively

slower pozzolanic reaction associated with calcined clay may continue to improve ITZ properties at later ages [80], which could influence fracture behavior at longer curing times. Future experiments should therefore extend the present methodology to concrete specimens with coarse aggregates and evaluate fracture energy, corrosion-induced cracking, and bond behavior at later curing ages.

In general, the results of this study demonstrate that fracture properties play a critical role in the development of corrosion-induced damage of cementitious systems. Based on these outcomes, a possible next step is to develop coupled numerical models that combine chloride ingress, corrosion propagation, rust expansion, and nonlinear fracture mechanics, calibrated using experimental data, such as the one generated in this work. Such models would enable more realistic service-life predictions for LC^3-based reinforced concrete structures.

Finally, despite the durability concerns highlighted in this work, the earlier occurrence of corrosion-induced cracking in LC^3 systems may also offer a practical advantage. Earlier cracking could act as an early warning indicator of corrosion activity before significant loss of steel cross-section has occurred, potentially allowing maintenance interventions to be implemented at an earlier and more cost-effective stage. This hypothesis should be examined through long-term structural exposure tests and monitoring under realistic environmental conditions.

References

[1] C. R. Gagg, "Cement and concrete as an engineering material: An historic appraisal and case study analysis", Eng. Fail. Anal. **40**, 114–140 (2014) (cit. on p. 1).

[2] R. M. Andrew, "Global CO_2 emissions from cement production", Earth Syst. Sci. Data **10**, 195–217 (2018) (cit. on p. 1).

[3] R. Snellings, P. Suraneni, and J. Skibsted, "Future and emerging supplementary cementitious materials", Cem. Concr. Res. **171**, 107199 (2023) (cit. on p. 1).

[4] A. Alujas Diaz, R. S. Almenares Reyes, T. Hanein, E. F. Irassar, M. Juenger, F. Kanavaris, M. Maier, A. T. Marsh, T. Sui, K.-C. Thienel, and et al., "Properties and occurrence of clay resources for use as supplementary cementitious materials: A paper of RILEM TC 282-CCL", Mater. Struct. **55**, 139 (2022) (cit. on p. 1).

[5] K. Scrivener, F. Martirena, S. Bishnoi, and S. Maity, "Calcined clay limestone cements (LC^3)", Cem. Concr. Res. **114**, Report of UNEP SBCI Working Group on low-CO_2 eco-efficient cement-based materials, 49–56 (2018) (cit. on pp. 2, 7).

[6] M. Sharma, S. Bishnoi, F. Martirena, and K. Scrivener, "Limestone calcined clay cement and concrete: A state-of-the-art review", Cem. Concr. Res. **149**, 106564 (2021) (cit. on p. 2).

[7] R. Gettu, A. Patel, V. Rathi, S. Prakasan, A. S. Basavaraj, S. Palaniappan, and S. Maity, "Influence of supplementary cementitious materials on the sustainability parameters of cements and concretes in the Indian context", Mater. Struct. **52**, 10 (2019) (cit. on p. 2).

[8] A. Poursaee and C. Hansson, "Potential pitfalls in assessing chloride-induced corrosion of steel in concrete", Cem. Concr. Res. **39**, 391–400 (2009) (cit. on p. 2).

[9] M. D. A. Thomas, "Durability of Concrete", in *Supplementary Cementing Materials in Concrete*, edited by M. D. A. Thomas (CRC Press, Boca Raton, FL, 2019) Chap. 9, pp. 151–208 (cit. on p. 2).

[10] M. D. A. Thomas and P. B. Bamforth, "Modelling chloride diffusion in concrete: Effect of fly ash and slag", Cem. Concr. Res. **29**, 487–495 (1999) (cit. on p. 2).

[11] V. G. Papadakis, “Effect of supplementary cementing materials on concrete resistance against carbonation and chloride ingress”, Cem. Concr. Res. **30**, 291–299 (2000) (cit. on p. 2).

[12] F. Lollini, E. Redaelli, and L. Bertolini, “Investigation on the effect of supplementary cementitious materials on the critical chloride threshold of steel in concrete”, Mater. Struct. **49**, 4147–4165 (2016) (cit. on p. 2).

[13] A. Ahmed, “Assessing the effects of supplementary cementitious materials on concrete properties: A review”, Discov. civ. eng. **1**, 145 (2024) (cit. on p. 2).

[14] P. Su, Q. Dai, and E. S. Kane, “Predicting chloride ingression in concrete containing different SCMs based on chloride binding and electrical resistivity”, Constr. Build. Mater. **414**, 134928 (2024) (cit. on p. 2).

[15] Y. Dhandapani, T. Sakthivel, M. Santhanam, R. Gettu, and R. G. Pillai, “Mechanical properties and durability performance of concretes with Limestone Calcined Clay Cement (LC^3)”, Cem. Concr. Res. **107**, 136–151 (2018) (cit. on pp. 2, 7).

[16] Y. Dhandapani, A. Machner, W. Wilson, W. Kunther, S. Afroz, T. Kim, F. Zunino, S. Joseph, F. Kanavaris, A. Castel, K. C. Thienel, E. F. Irassar, S. Bishnoi, F. Martirena, and M. Santhanam, “Performance of cementitious systems containing calcined clay in a chloride-rich environment: a review by TC-282 CCL”, Mater. Struct. **57**, 154 (2024) (cit. on pp. 2, 7, 22).

[17] Y. Dhandapani and M. Santhanam, “Assessment of pore structure evolution in the limestone calcined clay cementitious system and its implications for performance”, Cem. Concr. Compos. **84**, 36–47 (2017) (cit. on pp. 2, 7).

[18] H. Maraghechi, F. Avet, H. Wong, H. Kamyab, and K. Scrivener, “Performance of Limestone Calcined Clay Cement (LC^3) with various kaolinite contents with respect to chloride transport”, Mater. Struct. **51**, 125 (2018) (cit. on pp. 2, 7, 22).

[19] H.-L. Wang, J.-G. Dai, X.-Y. Sun, and X.-L. Zhang, “Characteristics of concrete cracks and their influence on chloride penetration”, Construct. Build. Mater. **107**, 216–225 (2016) (cit. on pp. 3, 30).

[20] *Eurocode 2: Design of Concrete Structures - Part 1-1: General Rules and Rules for Buildings*, European Standard EN 1992-1-1:2004 (European Committee for Standardization (CEN), Brussels, 2004) (cit. on pp. 3, 15).

[21] L. Bertolini, B. Elsener, P. Pedeferri, E. Redaelli, and R. Polder, *Corrosion of Steel in Concrete - Prevention, Diagnosis, Repair (2nd Edition)* (John Wiley & Sons, Weinheim, Germany, 2013) (cit. on p. 3).

[22] M. Pourbaix and R. W. Staehle, *Lectures on Electrochemical Corrosion* (Springer, Ney York, NY, 1973) (cit. on p. 4).

[23] P. Zhang, F. H. Wittmann, M. Vogel, H. S. Müller, and T. Zhao, "Influence of freeze-thaw cycles on capillary absorption and chloride penetration into concrete", Cem. Concr. Res. **100**, 60–67 (2017) (cit. on p. 4).

[24] S. Kessler, C. Thiel, C. U. Grosse, and C. Gehlen, "Effect of freeze-thaw damage on chloride ingress into concrete", Mater. Struct. **50**, 121 (2017) (cit. on p. 4).

[25] H. Kuosa, R. Ferreira, E. Holt, M. Leivo, and E. Vesikari, "Effect of coupled deterioration by freeze-thaw, carbonation and chlorides on concrete service life", Cem. Concr. Compos. **47**, Special issue: Durability of concrete, 32–40 (2014) (cit. on p. 4).

[26] Y. Li, R. wang, and Y. Zhao, "Effect of coupled deterioration by freeze-thaw cycle and carbonation on concrete produced with coarse recycled concrete aggregates", J. Ceram. Soc. Jpn. **125**, 36–45 (2017) (cit. on p. 4).

[27] B. Van Belleghem, S. Kessler, P. Van den Heede, K. Van Tittelboom, and N. De Belie, "Chloride induced reinforcement corrosion behavior in self-healing concrete with encapsulated polyurethane", Cem. Concr. Res. **113**, 130–139 (2018) (cit. on p. 4).

[28] J. Liao, X. Sun, Y. Wang, and Y. Wang, "Experimental and analytical investigation on chloride transport in LC3 and MPPF reinforced LC3 concrete considering the effect of transverse crack", Constr. Build. Mater. **482**, 141667 (2025) (cit. on p. 4).

[29] U. Angst, F. Moro, M. Geiker, S. Kessler, H. Beushausen, C. Andrade, J. Lahdensivu, A. Köliö, K. Imamoto, S. von Greve-Dierfeld, and M. Serdar, "Corrosion of steel in carbonated concrete: mechanisms, practical experience, and research priorities - a critical review by RILEM TC 281-CCC", RILEM Tech. Lett. **5**, 85–100 (2020) (cit. on p. 4).

[30] K. L. Scrivener, A. K. Crumbie, and P. Laugesen, "The Interfacial Transition Zone (ITZ) Between Cement Paste and Aggregate in Concrete", Interface Sci. **12**, 411–421 (2004) (cit. on pp. 4, 5).

[31] F. H. Wittmann, *Fracture Mechanics of Concrete*, Developments in Soil Science 7 (Elsevier, 1983) (cit. on p. 5).

[32] J. G. M. van Mier, *Fracture Processes of Concrete* (CRC Press, Boca Raton, FL, 1997), p. 464 (cit. on pp. 5, 6).

[33] Z. P. Bažant and J. Planas, *Fracture and Size Effect in Concrete and Other Quasibrittle Materials* (CRC Press, Boca Raton, FL, 1998) (cit. on pp. 5, 6).

[34] A. Hillerborg, M. Modéer, and P.-E. Petersson, "Analysis of crack formation and crack growth in concrete by means of fracture mechanics and finite elements", Cem. Concr. Res. **6**, 773–781 (1976) (cit. on p. 5).

[35] Z. P. Bažant, "Size Effect in Blunt Fracture: Concrete, Rock, Metal", J. Eng. Mech. **110**, 518–535 (1984) (cit. on p. 5).

[36] K. Lundgren, "Bond between ribbed bars and concrete. Part 2: The effect of corrosion", Mag. Concr. Res. **57**, 383–395 (2005) (cit. on pp. 6, 15–17, 25).

[37] K. Z. Hanjari, P. Utgenannt, and K. Lundgren, "Experimental study of the material and bond properties of frost-damaged concrete", Cem. Concr. Res. **41**, 244–254 (2011) (cit. on p. 6).

[38] K. Bhargava, A. Ghosh, Y. Mori, and S. Ramanujam, "Modeling of time to corrosion-induced cover cracking in reinforced concrete structures", Cem. Concr. Res. **35**, 2203–2218 (2005) (cit. on p. 6).

[39] M. Antoni, J. Rossen, F. Martirena, and K. Scrivener, "Cement substitution by a combination of metakaolin and limestone", Cem. Concr. Res. **42**, 1579–1589 (2012) (cit. on p. 6).

[40] J. Tang, S. H. Ma, W. F. Li, H. Yang, and X. D. Shen, "Research Progress on the Hydration of Portland Cement with Calcined Clay and Limestone", in Mater. Mach. Constr. Vol. 1036, Materials Science Forum (July 2021), pp. 240–246 (cit. on p. 6).

[41] A. Parashar and S. Bishnoi, "Hydration behaviour of limestone-calcined clay and limestone-slag blends in ternary cement", RILEM Tech. Lett. **6**, 17–24 (2021) (cit. on p. 6).

[42] J. Jiang, S. Sui, Z. Liu, F. Wang, and G. Geng, "Research on silicoaluminate-based low-carbon cementitious material–A state-of-the-art review", Fundam. Res. **5**, 2799–2814 (2025) (cit. on p. 6).

[43] Q. You, Z. Zhang, Y. Zheng, Y. Hu, Q. Liu, and G. Geng, "Steel passivation in LC^3 pore solution influenced by AFm deposition", Constr. Build. Mater. **505**, 144740 (2025) (cit. on p. 7).

[44] Y. Wang, Z. Xu, T. Mi, J. Yu, F. Xing, and W. Li, "Corrosion mechanism of reinforcement in LC3 cement pastes under coupled carbonation and chloride attack", Cem. Concr. Compos. **140**, 105080 (2023) (cit. on p. 7).

[45] R. Homayoonmehr, A. A. Ramezanianpour, F. Moodi, A. M. Ramezanianpour, and J. P. Gevaudan, "A Review on the Effect of Metakaolin on the Chloride Binding of Concrete, Mortar, and Paste Specimens", Sustainability **14**, 15022 (2022) (cit. on p. 7).

[46] Y. Dhandapani and M. Santhanam, "Investigation on the microstructure-related characteristics to elucidate performance of composite cement with limestone-calcined clay combination", Cem. Concr. Res. **129**, 105959 (2020) (cit. on p. 7).

[47] F. Zunino and K. Scrivener, "The reaction between metakaolin and limestone and its effect in porosity refinement and mechanical properties", Cem. Concr. Res. **140**, 106307 (2021) (cit. on p. 7).

[48] F. Avet and K. Scrivener, "Investigation of the calcined kaolinite content on the hydration of Limestone Calcined Clay Cement (LC^3)", Cem. Concr. Res. **107**, 124–135 (2018) (cit. on pp. 7, 22).

[49] R. Hay, L. Li, and K. Celik, "Shrinkage, hydration, and strength development of limestone calcined clay cement (LC^3) with different sulfation levels", Cem. Concr. Compos. **127**, 104403 (2022) (cit. on p. 7).

[50] F. Avet and K. Scrivener, "Influence of pH on the chloride binding capacity of Limestone Calcined Clay Cements (LC^3)", Cem. Concr. Res. **131**, 106031 (2020) (cit. on p. 7).

[51] M. S. H. Khan, Q. D. Nguyen, and A. Castel, "Carbonation of Limestone Calcined Clay Cement Concrete", in Calcined Clays for Sustainable Concrete, edited by F. Martirena, A. Favier, and K. Scrivener (2018), pp. 238–243 (cit. on p. 7).

[52] M. S. H. Khan, Q. D. Nguyen, and A. Castel, "Performance of limestone calcined clay blended cement-based concrete against carbonation", Adv. Cem. Res. **32**, 481–491 (2019) (cit. on p. 7).

[53] L. F. Salazar-Mayorga, J. M. Lizarazo-Marriaga, and J. F. Arango-Londoño, "Depassivation of reinforcing steel due to accelerated-carbonation in limestone calcined clay cement concretes", Mater. Struct. **58**, 5 (2024) (cit. on p. 7).

[54] Q. D. Nguyen and A. Castel, "Reinforcement corrosion in limestone flash calcined clay cement-based concrete", Cem. Concr. Res. **132**, 106051 (2020) (cit. on p. 7).

[55] S. Rengaraju, R. G. Pillai, L. Neelakantan, R. Gettu, and M. Santhanam, "Chloride-Induced Corrosion Resistance of Steel Embedded in Limestone Calcined Clay Cement Systems", in Calcined Clays for Sustainable Concrete, edited by S. Bishnoi (2020), pp. 613–619 (cit. on p. 7).

[56] European Committee for Standardization, *EN 196-1: Methods of testing cement - Part 1: Determination of strength*, tech. rep. (CEN, Brussels, Belgium, 2016) (cit. on p. 9).

[57] L. Cheng, R. Kurihara, T. Ohkubo, R. Kitagaki, A. Teramoto, Y. Suda, and I. Maruyama, "Plugging effect of fine pore water in OPC and LC^3 paste during accelerated carbonation monitored via single-sided nuclear magnetic resonance spectroscopy", Cem. Concr. Res. **186**, 107688 (2024) (cit. on p. 9).

[58] European Committee for Standardization, *EN 197-1: Cement - Part 1: Composition, specifications and conformity criteria for common cement*, tech. rep. (CEN, Brussels, Belgium, 2011) (cit. on p. 10).

[59] W. Feng, A. Tarakbay, S. Ali Memon, W. Tang, and H. Cui, "Methods of accelerating chloride-induced corrosion in steel-reinforced concrete: A comparative review", Construct. Build. Mater. **289**, 123165 (2021) (cit. on p. 11).

[60] J. Shi, J. Ming, and W. Sun, "Accelerated Corrosion Behavior of Steel in Concrete Subjected to Sustained Flexural Loading Using Electrochemical Methods and X-Ray Computed Tomography", J. Mater. Civ. Eng. **30**, 04018131 (2018) (cit. on p. 11).

[61] C. Alonso, C. Andrade, J. Rodriguez, and J. M. Diez, "Factors controlling cracking of concrete affected by reinforcement corrosion", Mater. Struct. **31**, 435–441 (1998) (cit. on p. 11).

[62] European Committee for Standardization, *EN 12390-3: Testing hardened concrete - Part 3: Compressive strength of test specimens*, tech. rep. (CEN, Brussels, Belgium, 2019) (cit. on p. 11).

[63] E. Brühwiler and F. H. Wittmann, "The wedge splitting test, a new method of performing stable fracture mechanics tests", Eng. Fract. Mech. **35**, Special Issue Fracture and Damage of Concrete and Rock, 117–125 (1990) (cit. on p. 11).

[64] NORDTEST, *NT BUILD 492: Concrete, mortar and cement-based repair materials: chloride migration coefficient from non-steady-state migration experiments*, tech. rep. (NORDTEST, Espoo, Finland, 1999) (cit. on p. 12).

[65] DIANA FEA BV, *DIANA FEA - Finite Element Analysis User's Manual, Release 10.10*, DIANA FEA BV (Delft, The Netherlands, 2025) (cit. on pp. 12, 14, 15).

[66] D. A. Hordijk, "Local Approach to Fatigue of Concrete", PhD thesis (Delft University of Technology, 1991) (cit. on p. 15).

[67] E. Thorenfeldt, A. Tomaszewicz, and J. J. Jensen, "Mechanical Properties of High-Strength Concrete and Application in Design", in Symposium Proceedings, Utilization of High-Strength Concrete (1987), pp. 149–159 (cit. on p. 15).

[68] A. Alhede, *User-Defined DIANA Subroutine for Corrosion Expansion Modelling*, Unpublished subroutine, private communication, 2024 (cit. on pp. 15, 16).

[69] A. Alhede, J. Dijkstra, A. Tengattini, and K. Lundgren, "Characterisation of steel corrosion and matrix damage in reinforced mortar combining analytical, electrical and image-based techniques", Cem. Concr. Res. **190**, 107792 (2025) (cit. on p. 16).

[70] S. Robuschi, A. Tengattini, J. Dijkstra, I. Fernandez, and K. Lundgren, "A closer look at corrosion of steel reinforcement bars in concrete using 3D neutron and X-ray computed tomography", Cem. Concr. Res. **144**, 106439 (2021) (cit. on p. 16).

[71] H. Sun, C. Jiang, K. Cao, D. Yu, W. Liu, X. Zhang, F. Xing, and D. Zhao, "Monitoring of steel corrosion and cracking in cement paste exposed to combined sulfate-chloride attack with X-ray microtomography", Construct. Build. Mater. **302**, 124345 (2021) (cit. on p. 16).

[72] M. Ghandehari, M. Zulli, and S. P. Shah, "Influence of Corrosion on Bond Degradation in Reinforced Concrete", in Fourteenth Engineering Mechanics Conference (May 2000) (cit. on pp. 16, 17).

[73] J. G. Cabrera and P. Ghoddoussi, "The effect of reinforcement corrosion on the strength of the steel/concrete 'bond'", in Bond in Concrete, Proceedings of an International Conference (1992) (cit. on pp. 16, 17).

[74] G. J. Al-Sulaimani, M. Kaleemullah, I. A. Basunbul, and Rasheeduzzafar, "Influence of Corrosion and Cracking on Bond Behavior and Strength of Reinforced Concrete Members", ACI Struct. J. **87**, 2 (1990) (cit. on pp. 16, 17).

[75] C. Andrade, C. Alonso, and F. J. Molina, "Cover cracking as a function of bar corrosion: Part I–Experimental test", Mater. Struct. **26**, 453–464 (1993) (cit. on pp. 16, 17).

[76] OriginLab Corporation, *OriginPro 2025*, Data analysis and graphing software. Northampton, MA, USA, 2024 (cit. on p. 24).

[77] A. Djerbi, S. Bonnet, A. Khelidj, and V. Baroghel-bouny, "Influence of traversing crack on chloride diffusion into concrete", Cem. Concr. Res. **38**, 877–883 (2008) (cit. on p. 30).

[78] X. Wang, M. Ba, B. Yi, and J. Liu, "Experimental and numerical investigation on the effect of cracks on chloride diffusion and steel corrosion in concrete", J. Build. Eng. **86**, 108521 (2024) (cit. on p. 30).

[79] A. Kumar, G. J. Singh, B. L. Chauhan, and R. Kumar, "Strength and Durability Performance of Recycled Aggregate Structural Concrete with Silica Fume, Furnace Slag, and M-Fine", J. Mater. Civ. Eng. **36**, 04024165 (2024) (cit. on p. 30).

[80] P. Duan, Z. Shui, W. Chen, and C. Shen, "Efficiency of mineral admixtures in concrete: Microstructure, compressive strength and stability of hydrate phases", Appl. Clay Sci. **83-84**, 115–121 (2013) (cit. on p. 31).